Edge Asymmetry Detection by Image Inversion in Coherent Imaging

Peng Kian Tan[1*] and Christian Kurtsiefer[1,2]
[1] *Centre for Quantum Technologies, 3 Science Drive 2, Singapore 117543 and*
[2] *Department of Physics, National University of Singapore, 2 Science Drive 3, Singapore, 117551*
(Dated: October 21, 2024)

Dark-field techniques are successfully used in microscopy for increasing the contrast of almost transparent objects, and for edge detection by removing image components with low spatial frequencies. A removal of image components with little interesting information but high intensity yields a higher signal-to-noise ratio for the image components of interest. Here, we present a technique to enhance the signal-to-noise ratio of an image signature contained in a spatial asymmetry. While being an interferometric technique based on image inversion, it will work with incoherent light sources, and thus be applicable in many practical imaging scenarios. We experimentally demonstrate an increase of the signal-to-noise ratio in edge asymmetry detection by an order of magnitude in a proof-of-principle experiment.

Keywords: Dark-Field, Edge Detection, Image Inversion, Incoherent Light, Spatial Asymmetry

I. DARK-FIELD IMAGING

A century ago, dark-field imaging in microscopy enabled the convenient observation of objects that scatter very little light by removing illumination components from the observation path that are not scattered by a specimen in a smart optical configuration [1]. As a result, the image formed by the light scattered from an object has a much higher contrast, or signal-to-noise ratio, than the corresponding image in a bright-field illumination.

In a more modern description, one could view this as a spatial filtering technique, that removes low frequency components of an image that contain little image information, but contribute to the background and thus noise in an observation. Dedicated spatial optical high pass filters can be used to enhance the edges of an object like the border of an almost transparent cell. Especially for objects with very little scattering, the removal of unscattered light might be the only way to have the signal level exceed the the noise level, ultimately given by the photon shot noise, of an unscattered background [2–5].

In the same spirit, we present an image inversion technique to enhance the signal-to-noise ratio in images where the information of interest is contained in a deviation from a spatial symmetry. The technique relies on an interferometric removal of symmetric image components by splitting the image information into two paths, and inverting the image in one of the paths. The interferometer can be arranged such that symmetric image components leave the interferometer through one port, while asymmetric image components are passed to the other port.

Similar techniques based on image inversion [6] have been predicted to outperform direct imaging in resolving sub-Rayleigh sources [7, 8], including for thermal light with a faint secondary source [9, 10]. Implementations have also been suggested in super-resolution microscopy [11], and towards astronomical coronagraphs [12–15].

* cqttpk@nus.edu.sg

II. IMAGE INVERSION SETUP

In our proof-of-principle demonstration illustrated in Fig. 1, we show that this interferometric removal of symmetric image content works for non-laser illumination sources, and thus might be of interest in applications seeking to identifiy an exoplanet passing by a much brighter star in astronomy, or in precision manufacturing process control.

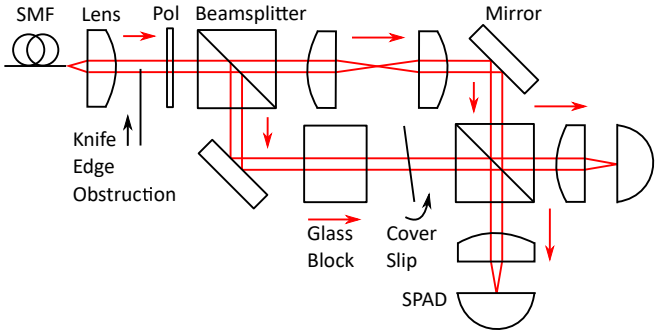

FIG. 1. Experimental setup for a Mach-Zehnder interferometer with radial image inversion. SMF: single-mode fiber, Pol: linear polariser, SPAD: single-photon avalanche detector. The setup is aligned to an interferometric visibility of V = 96 %.

The non-laser incoherent illumination is provided by a thermal light source generated from a low-pressure Mercury vapor gas discharge lamp. The light is spectrally filtered by a Fabry-Pérot etalon at the 546.1 nm emission line to increase its temporal coherence to around 0.5 ns for a corresponding coherent length of about 15 cm. This relaxes the requirement for zero optical path difference in the interferometer.

The light beam is then transmitted through a single-mode optical fiber to project into the fundamental Gaussian mode for spatial coherence, which is then collimated to a beam diameter around 2 mm. The beam is passed through a polariser to increase its interferometric visibility as orthogonal polarisation states do not interfere.

A non-polarising beamsplitter separates the incident beam into two, with one half passing through a pair of identical achromatic plano-convex lenses which perform the radial image inversion. The other half is passed through a 6.35 mm thick glass block to compensate for the optical path increase due to the two lens substrates.

The two beams are recombined at a second beamsplitter, with a 0.3 mm glass cover slip rotated to optimise for constructive and destructive interference fringes at the bright-field and dark-field output ports respectively, resulting in an interferometric visibility V = 96 %.

III. EDGE ASYMMETRY DETECTION

An edge asymmetry is introduced into the pupil plane of the optical path by a knife edge obstruction. The knife is linearly translated into the beam path in 10 μm steps from 0 mm to 2 mm, increasing the asymmetric image components, or optical modes, by $-N_A$ intensity. (Negative sign due to obstruction of light intensity)

The light intensities at the bright-field and dark-field output ports are measured by a pair of Silicon actively quenched single-photon avalanche detectors with a dark count rate of 1000 photoevents per second, and recorded by a field programmable gate array timestamp module.

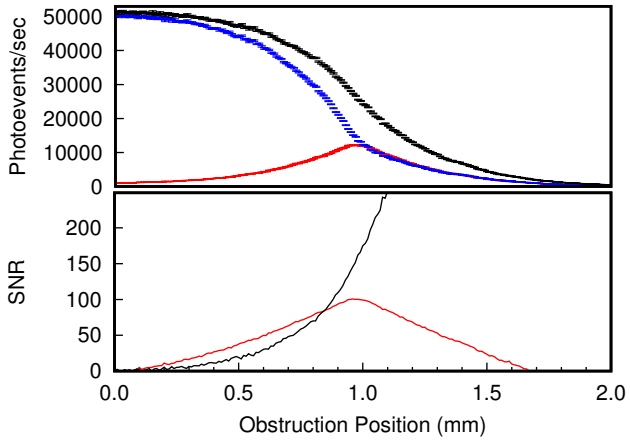

FIG. 2. Top: the output photoevents rate at the dark-field port $0.5N_A$ (red), bright-field port $N_S - 1.5N_A$ (blue), and combined intensity of $N_S - N_A$ (black). The combined intensity begins with only symmetric N_S modes due to the Gaussian beam from the single-mode optical fiber being radially symmetric. Bottom: the corresponding signal-to-noise ratios (SNR) for the edge asymmetry measurements with (red) versus without (black) image inversion.

When the obstruction position of the knife edge increases as shown in Fig. 2, the asymmetric spatial optical modes increasingly populate the dark-field output as the incident light decreases in radial symmetry about the optical axis of the image inversion lens pair.

The dark-field output increases at a rate of $0.5\,N_A$ due to the beamsplitting ratio of 50 : 50, because asymmetric spatial optical modes do not overlap after image inversion. The bright-field output decreases at a rate of $1.5\,N_A$ due to the other half of the beamsplitting ratio presenting $0.5\,N_A$ as before, in addition to the knife edge obstruction itself contributing another $1.0\,N_A$ factor.

At the half-way obstruction position around 1 mm, the two output intensities balance and then start to decrease at the same rate, as there is no longer any interferometric overlap by image inversion, and the light is therefore just transmitting through the second beamsplitter directly.

IV. GAIN IN SIGNAL-TO-NOISE RATIO

The expected gain G in the signal-to-noise ratio (SNR) for measuring the asymmetric optical modes N_A contribution may be described by the ratio between the signal-to-noise ratio with against without image inversion, or SNR_A against SNR_{S+A} respectively, as described by:

$$\begin{aligned} G &= \frac{SNR_A}{SNR_{S+A}} \\ &= \frac{(0.5 \times N_A)/\sqrt{0.5 \times N_A}}{N_A/\sqrt{N_S \pm N_A}} \\ &= \sqrt{0.5 \times \left(\frac{N_S}{N_A} \pm 1\right)} \end{aligned} \tag{1}$$

The asymmetric spatial optical modes do not overlap with themselves upon image inversion, and so transmit through the 50 : 50 beamsplitter without interference, resulting in the factor 0.5. The sign of $\pm$ depends on whether the edge asymmetry in image components is due to a light source (+), or an obstruction (−) as demonstrated in our proof-of-principle experiment.

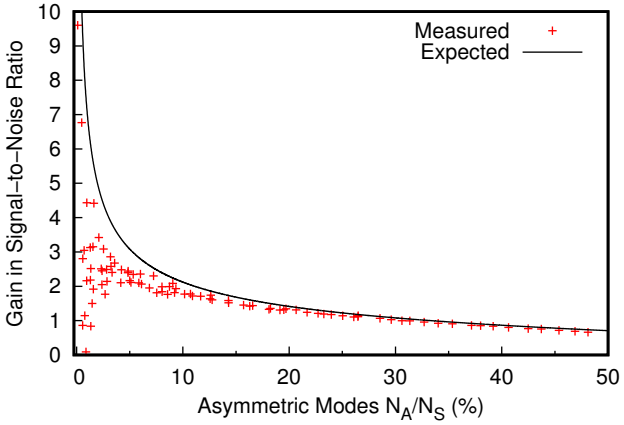

FIG. 3. Gain G in the signal-to-noise ratio of edge asymmetry detection in the image components (red points) in the experiment, compared to the model described by Eqn. 1 (black line).

As shown in Eqn. 1, the gain G in SNR increases inversely with the population of asymmetric modes N_A,

and is thus more significant for small asymmetric contributions N_A against a bright point source N_S. The gain in signal-to-noise ratio reduces to unity when the asymmetric-to-symmetric modes ratio is as follows:

$$N_A = -\frac{1}{3}N_S, \frac{1}{2}N_S \tag{2}$$

The measured gain in the signal-to-noise ratio for detecting asymmetric optical modes is shown in Fig. 3. It reduces to 1 as predicted by Eqn. 2 when the asymmetric modes N_A by obstruction is about 1/3 of the source original intensity N_S as a radially symmetric point of light emitting from a single-mode optical fiber.

V. FAR-FIELD COHERENCE PROPAGATION

We consider an outlook scenario where this image inversion technique might be potentially useful, such as the astrophysical context of a faint exoplanet transit across a bright star, and therefore introducing a small edge asymmetry in the object plane which may be weakly propagated in the far-field to the pupil plane of the observer.

The van Cittert–Zernike theorem states that the Fourier transform of the intensity distribution function at the source plane of a distant, spatially incoherent source is equal to its mutual coherence function Γ:

$$\Gamma_{12}(u,v,0) = \iint I(l,m)e^{-2\pi i(ul+vm)}dldm \tag{3}$$

where l and m are the direction cosines of a point on a distant source in the source plane, u and v are respectively the x-distance and the y-distance between the two observation points $(1,2)$ on the observation plane in unit of wavelength, and I is the intensity of the source.

The mutual coherence function Γ_{12} between two points 1 and 2 can then be normalized by the product of the square roots of the intensities $I_{1,2}$, and so yielding the complex degree of coherence γ_{12}:

$$\gamma_{12} = \frac{\Gamma_{12}}{\sqrt{I_1}\sqrt{I_2}} \tag{4}$$

The interferometric visbility V is given by the modulus of the complex degree of coherence γ, and so

$$|\gamma_{12}| = V \tag{5}$$

Because the mutual coherence function Γ is a Fourier transform of the source intensity distribution, and Fourier transformation is a linear operation, thus

$$\Gamma_{star-spot} = \Gamma_{star} - \Gamma_{spot} \tag{6}$$

The intensity distributions of a star and a planet are both assumed to be discs, and so the Fourier transforms lead to Bessel functions of the form where θ is small, weighted by the respective source (or obstructed) intensity I:

$$\Gamma = I\frac{2J_1(ka\theta)}{ka\theta} \tag{7}$$

where J_1 is the Bessel function of the first kind of order one, $k = 2\pi/\lambda$ is the wavenumber, a is the radius of the telescope aperture, and θ is the angular extent of the star or spot. This leads to the combined mutual coherence:

$$\Gamma_{star-spot} = I_{star}\frac{2J_1(ka\theta_{star})}{ka\theta_{star}} - I_{spot}\frac{2J_1(ka\theta_{spot})}{ka\theta_{spot}}e^{-ikacos\delta} \tag{8}$$

The exponential term on the right is a shift function resulting from the Fourier transform of an intensity distribution (obstruction) that is slightly off-axis by a small angle δ, given by the angular radius of the star, e.g. 0.0025 arcseconds for Sirius.

The measurable visibility $V_{star-spot}$ for an obstructed star is the modulus of the coherence function normalised by the incident intensity:

$$V = \frac{1}{I_{star-spot}}\left|I_{star}\frac{2J_1(ka\theta_{star})}{ka\theta_{star}} - I_{spot}\frac{2J_1(ka\theta_{spot})}{ka\theta_{spot}}e^{-ikacos\delta}\right| \tag{9}$$

compared against that of the star itself:

$$V_{star} = \frac{1}{I_{star}}\left|I_{star}\frac{2J_1(ka\theta_{star})}{ka\theta_{star}}\right| \tag{10}$$

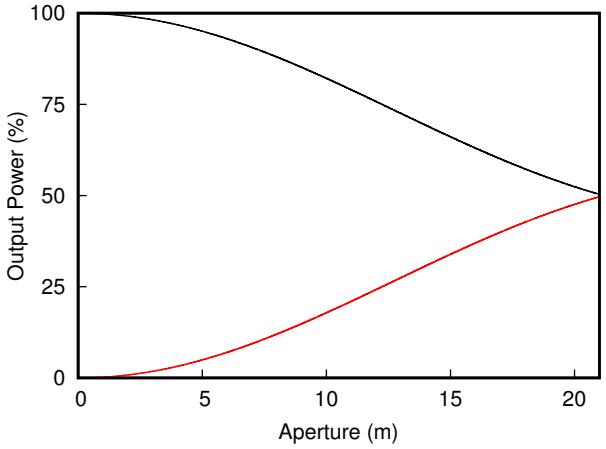

FIG. 4. Output power distribution into the asymmetric mode (red) and symmetric mode (black) without obstruction. Assuming the light source to be Sirius, and the obstruction to be Jupiter, for scaling their angular sizes and obstructed intensity. The symmetric and asymmetric output power both approach 50%, or zero visibility, with increasing aperture size as a 21 metre aperture would resolve Sirius in imaging. Mean wavelength λ assumed to be 500 nm for this toy model.

In our image inversion setup that separates into symmetric (Sym) and asymmetric (Asym) mode outputs, the corresponding interferometric visibility is:

$$V = \frac{Sym - Asym}{Sym + Asym} \tag{11}$$

where the total intensity as normalisation for simplicity

$$Sym + Asym = 1 \tag{12}$$

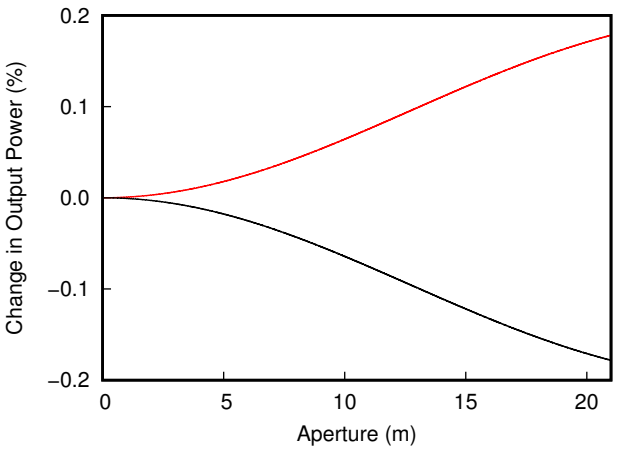

FIG. 5. The power changes in the asymmetric (red) and symmetric (black) modes in the event of an obstruction.

and so leading to the fractional power splitting between the symmetric and asymmetric outputs to be

$$Sym = V/2 + 0.5 \tag{13}$$

and

$$Asym = 0.5 - V/2 \tag{14}$$

The output power splitting plotted in Fig. 4 is thus determined by the instrument interferometric visibility.

This suggests that that spatial asymmetry in the target of interest do propagate in the far-field regime, and may be detectable even when the optical aperture is diffraction limited to directly image the asymmetrical content.

However, decreasing aperture size would reduce both the signal and the noise components in the asymmetric mode detection. This constrains the regime whereby there is a net gain in signal-to-noise, which agrees with the trend observed in our results shown in Fig. 3, and is dependent on the interferometric visibility of the instrument, and the spatial symmetry distribution of the target of interest.

VI. ACKNOWLEDGMENTS

This research is supported by the Quantum Engineering Programme through NRF2021-QEP2-03-P02, the Ministry of Education and the National Research Foundation, Prime Minister's Office, Singapore.

[1] J. J. Lister, On some properties in achromatic object-glasses applicable to the improvement of the microscope, Philos. Trans. Royal Society **120**, 187 (1830).
[2] O. Guyon, C. Roddier, J. E. Graves, F. Roddier, S. Cuevas, C. Espejo, S. Gonzalez, A. Martinez, G. Bisiacchi, and V. Vuntesmeri, The nulling stellar coronagraph laboratory tests and performance evaluation, PASP **111**, 1321 (1999).
[3] S. Itoh, T. Matsuo, S. Goda, H. Shibai, and T. Sumi, Pupil masks for spectrophotometry of transiting exoplanets, AJ **154**, 97 (2017).
[4] T. Currie, E. Pluzhnik, O. Guyon, R. Belikov, K. Miller, S. Bos, J. Males, D. Sirbu, C. Bond, R. Frazin, T. Groff, B. Kern, J. Lozi, B. A. Mazin, B. Nemati, B. Norris, H. Subedi, and S. Will, Laboratory demonstration of spatial linear dark field control for imaging extrasolar planets in reflected light, PASP **132**, 104502 (2020).
[5] K. L. Miller, S. P. Bos, J. Lozi, O. Guyon, D. S. Doelman, S. Vievard, A. Sahoo, V. Deo, N. Jovanovic, F. Martinache, F. Snik, and T. Currie, Spatial linear dark field control on subaru scexao maintaining high contrast with a vapp coronagraph, A&A **646**, 12 (2021).
[6] M. Tsang, R. Nair, and X.-M. Lu, Quantum theory of superresolution for two incoherent optical point sources, Phys. Rev. X **6**, 031033 (2016).
[7] M. Tsang, Resolving starlight a quantum perspective, Contemporary Physics **60**, 279 (2019).
[8] Z. S. Tang, K. Durak, and A. Ling, Fault-tolerant and finite-error localization for point emitters within the diffraction limit, Opt. Express **24**, 22004 (2016).
[9] Z. Huang and C. Lupo, Quantum hypothesis testing for exoplanet detection, Phys. Rev. Lett. **127**, 130502 (2021).
[10] F. Allouche, A. Glindemann, E. Aristidi, and F. Vakili, Absolute position interfero coronagraph for direct exoplanet detection, A&A **500**, 1277 (2009).
[11] A. A. Pushkina, G. Maltese, J. I. C. Filho, P. Patel, and A. I. Lvovsky, Superresolution linear optical imaging in the far field, Phys. Rev. Lett **127**, 253602 (2021).
[12] E. Serabyn, K. Liewer, and G. Ruane, Geometric phase based phase knife mask for stellar nulling and corongraphy, Opt. Express **32**, 19924 (2024).
[13] A. V. Tavrov, J. Nishikawa, M. Tamura, L. Abe, K. Yokochi, T. Kurokawa, and M. Takeda, Common-path achromatic interferometer-coronagraph images from a breadboard demonstrator, Appl. Opt. **46**, 6885 (2007).
[14] A. V. Tavrov, O. I. Korablev, A. V. Rodin, I. I. Vinogradov, A. Y. Trokhimovsky, A. Y. Ivanov, L. V. Ksanfomaliti, and D. A. Orlov, Stellar coronagraph using the principle of achromatic null-interferometer, Cosmic Research **49**, 99 (2011).
[15] A. Tavrov, S. Kameda, A. Yudaev, I. Dzyuban, A. Kiselev, I. Shashkova, O. Korablev, M. Sachkov, J. Nishikawa, M. Tamura, G. Murakami, K. Enya, M. Ikoma, and N. Narita, Stellar imaging coronagraph and exoplanet coronal spectrometer two additional instruments for exoplanet exploration onboard the wso uv 1.7m orbital telescope, JATIS **4**, 044001 (2018).